# Focusing Highly Squinted FMCW-SAR Data Using the Modified Wavenumber-Domain Algorithm

Tinghao Zhang, *Graduate Student Member, IEEE*, Yachao Li, *Member, IEEE*, Mingze Yuan, Liang Guo, *Member, IEEE*, Jiao Guo, Hao Lin, *Member, IEEE*, and Mengdao Xing, *Fellow, IEEE*

***Abstract*—The three-dimensional (3-D) acceleration, azimuth dependence, and real-time processing are the main issues to be solved in highly squinted frequency-modulation continuous-wave (FMCW) synthetic aperture radar (SAR) with a curved trajectory. To overcome these issues, a modified wavenumber-domain algorithm is developed in this article. The proposed modified wavenumber-domain algorithm mainly includes the following six aspects. First, a modified range model considering 3-D acceleration for a curved trajectory is established. Then, the spectrum compression and rotation operations are performed to guarantee further processing. Afterward, residual phase terms introduced by acceleration are bulk compensated for. Moreover, the azimuth dependence is eliminated by the azimuth resampling to achieve uniform focusing. Subsequently, the range–azimuth coupling is removed by the modified Stolt interpolation. Finally, to avoid image aliasing, the azimuth wavenumber domain is selected to focus the final image. The experimental results of both numerical and raw-measured FMCW-SAR data demonstrate the superiority of the proposed method.**

***Index Terms*—Curved trajectory, frequency-modulation continuous-wave (FMCW), wavenumber domain.**

## I. Introduction

SYNTHETIC aperture radar (SAR) plays an increasingly significant role in civil topographic mapping due to its all-weather and all-time capabilities [1], [2]. With the rapid development of SAR technology, the SAR system has been widely applied to high-speed maneuvering platforms, such as airplanes, missiles, and unmanned aerial vehicles [3], [4], [5], [6], [7], [8], [9], [10], [11], [12], [13], for airplane navigation, terminal guidance, and autonomous landing of interesting areas. However, with the increasing demand for civil surveying and mapping fields, the SAR system requires compact size, lightweight, and low cost [14], which is suitable for frequency-modulation continuous-wave (FMCW) SAR.

Different from the conventional pulsed SAR, the start–stop approximation will not be held in FMCW-SAR because there exists the variation of the range history caused by the continuous motion during the pulse time, which means that the leading edge and the trailing edge of any transmitted pulse will experience different delay times. Consequently, the conventional pulsed SAR algorithms cannot immediately be applied to FMCW SAR due to the additional range walk and range-coupling terms. In addition, the cases of high-squint angle, azimuth dependence of Doppler parameters, real-time processing, and curved trajectory must also be considered.

For instance, when FMCW-SAR works at high-squint mode, the range–azimuth coupling of the echo signal is generally severe [15], which leads to the difficulty of SAR focusing. To solve this problem, the modified range-Doppler algorithm (RDA) [16] uses the modified range migration correction method to compensate for the continuous motion within the sweep and utilizes improved secondary range compression to mitigate range coupling. However, RDA cannot remove the high-order coupling phase terms, which will degrade the final imaging quality. Therefore, several chirp scaling algorithms [17] are proposed and successfully improve the high-squint SAR imaging performance. Especially, Meta et al. [18] proposed a modified frequency-domain method to correct the Doppler shift in the FMCW-SAR. In addition, to solve the issue of the azimuth dependence, some nonlinear chirp scaling (NCSs) [19], [20], [21], [22], [23] are developed and effectively eliminated the azimuth dependence of the Doppler parameters. Unfortunately, these methods are only suitable for full-aperture data processing. In order to meet the requirement of real-time processing, the subaperture data processing approach is more attractive. Therefore, Liang et al. [24] proposed an extended NCS approach combined with spectrum analysis to achieve small-aperture data processing. However, the spatial-variation (SV) range cell migration (RCM) is ignored in this work. Consequently, the final image-focused performance needs to be further improved.

On the other hand, the Stolt interpolation [25], [26], [27], [28], [29] is an excellent choice to correct the SV RCM without approximation. However, in the high-squint FMCW-SAR mode, an extra range–azimuth coupling phase term exists due to the continuous motion. Therefore, Wang et al. [30] proposed the wavenumber-domain method to focus high-squint FMCW-SAR

Manuscript received 16 February 2023; revised 20 March 2023; accepted 6 April 2023. Date of publication 13 April 2023; date of current version 28 December 2023. This work was supported in part by the National Key R&D Program of China under Grant 2018YFB2202500 and Grant 2018YFB2202505; in part by the Science Foundation for Distinguished Young Scholars of Shaanxi Province under Grant 2020JC-25; and in part by the National Key R&D Program of Shaanxi Province under Grant 2017ZDXM-SF-094. *(Corresponding author: Yachao Li.)*

Tinghao Zhang, Yachao Li, Mingze Yuan, Liang Guo, Hao Lin, and Mengdao Xing are with the National Laboratory of Radar Signal Processing, Xidian University, Xi'an 710071, China, and also with the Collaborative Innovation Center of Information Sensing and Understanding, Xidian University, Xi'an 710071, China (e-mail: tinghaozth@163.com; ycli@mail.xidian.edu.cn; mingzeyuan@stu.xidian.edu.cn; lguo@mail.xidian.edu.cn; 1594565140@qq.com; xmd@xidian.edu.cn).

Jiao Guo is with the College of Mechanical and Electronic Engineering, Northwest A&F University, Yangling 712100, China (e-mail: jiao.g@163.com).

Digital Object Identifier 10.1109/JSTARS.2023.3266886

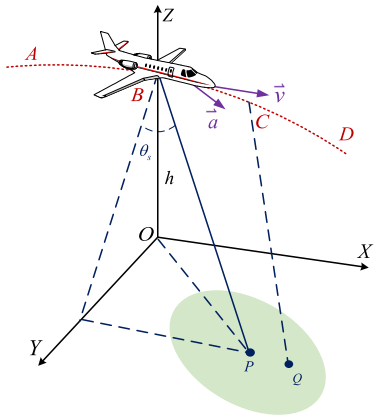


Fig. 1. Geometry of highly squinted FMCW-SAR with a curved trajectory.

data. But its range model is established on a straight trajectory with a constant velocity, which means it will be invalid when the SAR platform moves along with a curved trajectory. Consequently, the variation of velocity should be considered in the range model. Although some previous range models, such as the hyperbolic range equation, equivalent squint range model, and their extensions [31], [32], [33], [34], considered the variation of velocity, these models exist residual phase error that cannot be ignored in the case of highly squinted FMCW-SAR with a curved trajectory. Therefore, some time-domain imaging algorithms [35], [36], [37], [38], [39] are proposed to realize well focusing based on the accurate coherent integral, which is theoretically applicable to arbitrary trajectory. However, the vast computation burden limits the practical application of these time-domain algorithms.

Motivated by the discussion above, this article develops a modified wavenumber-domain algorithm for highly squinted FMCW-SAR with a curved trajectory. First, a modified range model considering three-dimensional (3-D) acceleration is established and analyzed in detail. Then, spectrum compression (SC) and rotation processing are performed to mitigate acceleration impacts and realize the maximum 2-D WS utilization. Afterward, the residual phase terms introduced by the 3-D acceleration are bulk compensated for. After that, the azimuth dependence is eliminated by the azimuth resampling to achieve uniform focusing. Subsequently, the modified Stolt interpolation removes the range–azimuth coupling phase terms. Finally, the final image is focused on the azimuth wavenumber domain through the data aligning processing, which can avoid numerous zero-padding operations.

The rest of this article is organized as follows. In Section II, we deeply describe the echo signal model with 3-D acceleration. Section III introduces the proposed method. Section IV presents the computational load of the proposed method. The results of numerical simulation and raw-measured SAR data processing are shown in Section V. Finally, Section VI concludes this article.

## II. Echo Signal Model

Fig. 1 shows the highly squinted imaging configuration of FMCW-SAR with a curved trajectory. The SAR platform moves along the curvilinear descending $\widehat{ABD}$ during the synthetic aperture time $t_a$ with the velocity vector $\vec{v} = (v_x, 0, v_z)$ and the acceleration vector $\vec{a} = (a_x, a_y, a_z)$ in the coordinates $O - XYZ$, respectively. At this time, $B(0, 0, h)$ is the position corresponding to the azimuth time $t_a = 0$, and point $C$ is the arbitrary position within the $\widehat{ABD}$.

From Fig. 1, the instantaneous range of point $Q$ can be expressed as follows:

$$R(t_r, t_a, R_0) = \sqrt{\begin{aligned}&\left(v_x(t_a+t_r)+\tfrac{1}{2}a_x(t_a+t_r)^2 - v_x t_n - \tfrac{1}{2}a_x t_n^2 - R_0\sin\theta_s\right)^2 \\ &+\left(v_z(t_a+t_r)+\tfrac{1}{2}a_z(t_a+t_r)^2 - v_z t_n - \tfrac{1}{2}a_z t_n^2 + h\right)^2 \\ &+\left(\tfrac{1}{2}a_y(t_a+t_r)^2 - \tfrac{1}{2}a_y t_n^2 - \sqrt{(R_0\cos\theta_s)^2 - h^2}\right)^2\end{aligned}} \tag{1}$$

where $t_a$ denotes the azimuth slow time and $t_r$ represents the range fast time. $\theta_s$ denotes the squint angle. $R_0$ is the slant range from position $B$ to target $P$. $t_n$ denotes the zero-Doppler time.

Due to the complicated expression of (1), the 2-D WS is hard to obtain. Therefore, according to the Taylor series expansion, the instantaneous slant range can be expressed as follows:

$$R(t_r, t_a, R_0) \approx R_0 + \sum_{i=1}^{4} k_i(R_0, t_n)(t_a + t_r - t_n)^i \tag{2}$$

where $k_i(R_0) = (1/i!)(d^i R(t_r, t_a, R_0)/dt_a^i|_{t_a=t_n-t_r})$ represents the coefficient of the Taylor series.

However, the Taylor coefficients $k_i$ cannot directly display the impacts of 3-D acceleration. Consequently, according to the ideal of motion compensation, (2) can be divided into acceleration term and nonacceleration term, which yields

$$\begin{aligned}&R(t_r, t_a, R_0) \\ &= \sqrt{(R_0\sin\theta_e - (v(t_a+t_r) - vt_n))^2 + (R_0\cos\theta_e)^2} \\ &\quad + \sum_{i=2}^{4} A_{ai}(R_0)(t_a - t_n)^i + \Delta R(t_r, \vec{a})\end{aligned} \tag{3}$$

where $v = (v_x^2 + v_z^2)^{1/2}$ and $v\sin\theta_e = v_x\sin\theta_s + v_z\cos\varphi$. $\varphi$ is the angle between the height and slant range. $\theta_e$ denotes the equivalent squint angle. $A_{ai}$ are the high-order coefficients related to the 3-D acceleration.

From (3), the first component represents the traditional hyperbolic range model; the other parts denote the residual components caused by acceleration. To further analyze the characterization of the range model, based on the parameters in Table I, the numerical experimental simulation of the third part is performed, and the results are shown in Fig. 2. From Fig. 2, it is obvious that the envelope error is far less than a quarter of range unit and the phase error is less than its critical value $\pi/4$. It means that the third part in (3) can be neglected. Consequently, the range

TABLE I
SYSTEM PARAMETERS

| Parameters | Values | Parameters | Values |
|---|---|---|---|
| Carrier frequency | 35 GHz | Height | 1 km |
| PRF | 1.6 kHz | Squint angle | 70° |
| Range bandwidth | 1.2 GHz | Slant range | 4 km |
| Velocity | $(180, 0, -22)$ m/s | Acceleration | $(0.8, 0.2, -3.8)$ m/s$^2$ |

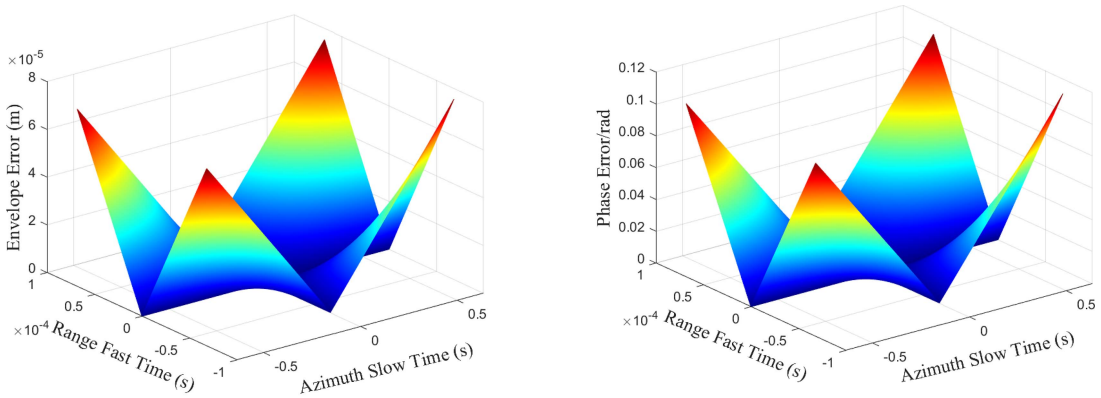


(a) (b)

Fig. 2. Result of envelope and phase error. (a) Envelope error. (b) Phase error.

model (3) can be rewritten as

$$R(t_r, t_a, R_0) = \sqrt{(R_0 \sin\theta_e - (v(t_a + t_r) - vt_n))^2 + (R_0 \cos\theta_e)^2} + \sum_{i=2}^{4} A_{ai}(R_0)(t_a - t_n)^i. \quad (4)$$

Suppose the received signal is given by

$$ss(t_r, t_a) = w(t_r) \cdot w(t_a) \cdot \exp\left(\begin{array}{l} -j\frac{4\pi}{\lambda}(R(t_r, t_a, R_0) - R_{\text{ref}}) \\ -j\frac{4\pi}{c}\gamma(R(t_r, t_a, R_0) - R_{\text{ref}})\Delta t_r \\ +j\frac{4\pi}{c^2}\gamma(R(t_r, t_a, R_0) - R_{\text{ref}})^2 \end{array}\right) \quad (5)$$

where $w_r(t_r)$ and $w_a(t_a)$ denote the range envelope and the azimuth envelope, respectively; they will be omitted in the following derivation: $\Delta t_r = t_r - 2R_{\text{ref}}/c$, $f_c$ represents the carrier frequency, $c$ denotes the speed of light, $\gamma$ is the range chirp rate, and $R_{\text{ref}}$ is the reference slant range.

After RVP correcting [31], the echo signal becomes

$$Ss(k_r, X_a) = \exp(-jk_r(R(X_r, X_a, R_0) - R_{\text{ref}})) \quad (6)$$

with

$$R(X_r, X_a, R_0) = \sqrt{R_0^2 + (X_r + X_a - X_n)^2 - 2R_0 \sin\theta_e (X_r + X_a - X_n)} + \sum_{i=2}^{4} A_{ai}^*(R_0)(X_a - X_n)^i \quad (7)$$

where $k_r = 4\pi(f_c + f_r)/c$ and $A_{ai}^* = A_{ai}/v$.

## III. MODIFIED WAVENUMBER-DOMAIN ALGORITHM

There are three main aspects that should be considered before using the wavenumber-domain algorithm. The first is eliminating acceleration effects and maintaining higher 2-D WS utilization. The second is the spectrum rotation that will cause the azimuth dependence problem. The last is the small-aperture processing without padding zeros. After that, the wavenumber-domain algorithm can be solved to the highly squinted FMCW-SAR with curved trajectory imaging problems. Now, the solutions to these aspects will be further discussed in detail as follows.

### A. SC and Rotation

In the highly squinted FMCW-SAR with a curved trajectory, 3-D acceleration will result in azimuth bandwidth exceeding its azimuth support domain, as shown in Fig. 3(a), which is unsuitable for further 2-D WS processing. Therefore, the SC

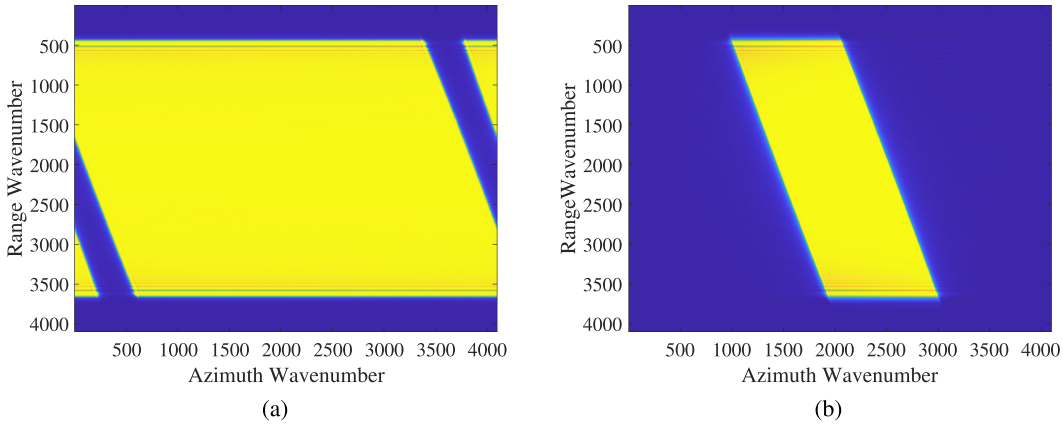


Fig. 3. Two-dimensional wavenumber spectrum. (a) Before compression. (b) After compression.

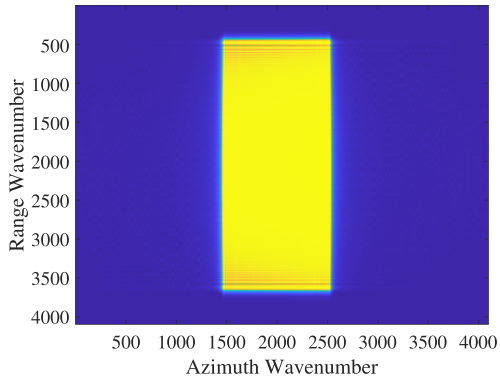


Fig. 4. Result of SC and rotation.

operation is adopted to eliminate the impact of acceleration, which yields

$$H_{\mathrm{sc}}\left(k_r, X_a\right)=\exp\left(jk_r\cdot A_{a2}^{*}\left(R_{\mathrm{ref}}\right)X_a^2\right). \tag{8}$$

Fig. 3(b) shows the result of SC. However, the skew wavenumber spectrum (SWS) characteristic remains. In order to achieve Stolt interpolation, a rectangular region needs to be selected in the WS. One way to obtain a rectangular WS is to select an inscribed rectangle region in SDSR. Another way is to choose a circumscribed rectangle region out of the SWS. But both two ways will degrade the final image-focusing performance

One way to deal with this issue is to correct the SWS into a rectangle WS, which is equivalent to rotating the SWS. The maximum WS utilization rate is realized. However, it will introduce interpolation errors. Fortunately, the linear range walk correction can achieve the same effect. Consequently, the wavenumber spectrum rotation (WSR) factor is

$$H_{\mathrm{wsr}}\left(k_r, X_a\right)=\exp\left[-jk_r\left(X_r+X_a\right)\sin\theta_e\right]. \tag{9}$$

The result of WSR is given in Fig. 4, and the signal is renovated as

$$Ss\left(k_r, X_a\right)=\exp\left(-jk_r\sqrt{\begin{array}{l}R_0^2+\left(X_a+X_r-x_n\right)^2\\-2R_0\sin\theta_e\left(X_a+X_r-x_n\right)\end{array}}\right)$$
$$\cdot\exp\left(-jk_r\left(X_a+X_r\right)\sin\theta_e\right)$$
$$\cdot\exp\left(-jk_r\left(A_{a2}^{*}\left(R_0\right)-A_{a2}^{*}\left(R_{\mathrm{ref}}\right)\right)\left(X_a-x_n\right)^2\right)$$
$$\cdot\exp\left(-jk_r\cdot\sum_{i=3}^{4}A_{ai}^{*}\left(R_0\right)\left(X_a-x_n\right)^i\right)$$
$$\cdot\exp\left(-jk_r\cdot A_{a2}^{*}\left(R_{ref}\right)x_n^2\right)$$
$$\cdot\exp\left(j2k_r\cdot A_{a2}^{*}\left(R_{\mathrm{ref}}\right)X_a\cdot x_n\right)$$
$$\cdot\exp\left(jk_rR_{\mathrm{ref}}\right). \tag{10}$$

Observing the phase terms of (10), the first part denotes the traditional phase term without acceleration. Spectrum rotation processing introduces the second part. The third part represents the residual phase components introduced by SC. The fourth part denotes the residual high-order phase term, and the other components will be eliminated in the further processing.

### B. Residual Phase Components Compensation

After applying azimuth fast Fourier transform (FFT), the signal (10) is renovated as follows:

$$SS\left(k_r, k_x\right)=\exp\left(\begin{array}{c}-jR_0\sqrt{k_r^2-\left(k_x+k_r\sin\theta_e-k_n\right)^2}\cos\theta_e\\-j\left(R_0\sin\theta_e-X_r+x_n\right)\left(k_x+k_r\sin\theta_e\right)\\-jk_r\left(A_{a2}^{*}\left(R_0\right)-A_{a2}^{*}\left(R_{\mathrm{ref}}\right)\right)X'^2\\-jk_r\cdot\sum_{i=3}^{4}A_{ai}^{*}\left(R_0\right)X'^i-jk_r\cdot A_{a2}^{*}\left(R_{\mathrm{ref}}\right)x_n^2\\+jk_nR_0\sin\theta_e+jk_nx_n+j\frac{k_n}{2}X'+jk_rR_{\mathrm{ref}}\\-jk_rX_r\sin\theta_e\end{array}\right) \tag{11}$$

with

$$X'=R_0\sin\theta_e-\frac{R_0\cos\theta_{\mathrm{e}}}{\sqrt{k_r^2-\left(k_x-k_n+k_r\sin\theta_e\right)^2}}\left(k_x-k_n+k_r\sin\theta_e\right) \tag{12}$$

where $k_x = 2\pi f_a / v$ and $k_n = 2k_r \cdot A^*_{a2}(R_{\text{ref}})x_n$. Applying Taylor expansion of $k_n = 0$, (12) becomes

$$\begin{aligned} &SS\left(k_r, k_x\right) \\ &= \exp\left(-jR_0\sqrt{k_r^2 - \left(k_x + k_r \sin\theta_e\right)^2}\cos\theta_e\right) \\ &\cdot \exp\left(-j\left(k_x + k_r\sin\theta_e\right)\left(R_0\sin\theta_e + x_n\right)\right) \\ &\cdot \exp\left(jk_xX_r + jk_rR_{\text{ref}}\right) \\ &\cdot \exp\begin{pmatrix} -jk_r\left(A^*_{a2}\left(R_0\right) - A^*_{a2}\left(R_{\text{ref}}\right)\right)X^{*2} \\ -jk_r\cdot\sum_{i=3}^{4}A^*_{ai}\left(R_0\right)X^{*i}\end{pmatrix} \\ &\cdot \exp\left(j2R_0\sin\theta_e\cdot k_n + j\frac{3k_n}{2}x_n\right) \end{aligned} \tag{13}$$

with

$$X^* = R_0\sin\theta_e - \frac{R_0\cos\theta_e}{\sqrt{k_r^2 - \left(k_x + k_r\sin\theta_e\right)^2}}\left(k_x + k_r\sin\theta_e\right) \tag{14}$$

From (13), the first phase term denotes an analytical WS; the second phase term is introduced by the spectrum rotation operation; the third exponential term can be directly compensated for in the next derivation; the fourth phase term denotes the high-order residual term; and the fifth phase term is the residual term of distortion.

In order to eliminate the impacts of residual high-order phase terms introduced by the acceleration, a bulk compensation function is given as follows:

$$\begin{aligned} H_{\text{bulk}}\left(k_r, X^*\right) = &\prod_{i=3}^{4}\exp\left(j\left(A^*_{ai}\left(R_{\text{ref}}\right)X^{*i}\right)k_r\right) \\ &\cdot\exp\left(-j\left(k_xX_r + k_rR_{\text{ref}}\right)\right). \end{aligned} \tag{15}$$

Through the high-order phase compensation, the signal is renovated as

$$\begin{aligned} &SS\left(k_r, k_x\right) \\ &= \exp\begin{pmatrix} -jR_0\cos\theta_e\sqrt{k_r^2\cos^2\theta_e - 2k_rk_x\sin\theta_e - k_x^2} \\ -j\left(R_0\sin\theta_e + x_n\right)\left(k_x + k_r\sin\theta_e\right) \\ -jk_r\cdot\sum_{i=2}^{4}\left(A^*_{ai}\left(R_0\right) - A^*_{ai}\left(R_{\text{ref}}\right)\right)X^{*i} \\ +j2R_0\sin\theta_e\cdot k_n + j\frac{3k_n}{2}x_n\end{pmatrix}. \end{aligned} \tag{16}$$

For further analysis, (16) is rewritten as

$$\begin{aligned} &SS\left(k_r, k_x\right) \\ &= \exp\begin{pmatrix} -jR_0\cos\theta_e\sqrt{k_r^2\cos^2\theta_e - 2k_rk_x\sin\theta_e - k_x^2} \\ -j\left(R_0\sin\theta_e + x_n\right)\left(k_x + k_r\sin\theta_e\right) \\ +j\psi_{\text{res}}\left(k_r, k_x\right) + j\xi\left(k_r, x_n\right)\end{pmatrix} \end{aligned} \tag{17}$$

where

$$\psi_{\text{res}}\left(k_r, k_x\right) \approx \psi\left(k_{rc}, k_x\right) + \psi\left(\Delta k_r, k_x\right) \tag{18}$$

$\psi_{\text{res}}(k_r, k_x)$ denotes the disturbance component introduced by the 2D-WS approximation, and $\xi(k_r, x_n)$ denotes the image deformation, which has no impact on the image focusing and can be ignored in the following analysis. $\varphi(\Delta k_r, k_x)$ represents the residual envelope. For further analysis, the simulation is made, as shown in Fig. 5, and the simulation parameters are shown in Table I.

From the above simulation results, we can see that the maximum residual envelope error is far less than a quarter of the range cell, and the maximum residual phase error exceeds $\pi/4$. Therefore, the effect of the residual envelope error can be ignored, while the impact of residual phase error should be considered. Consequently, the residual phase error compensation function can be given by

$$H_{\text{res}}\left(k_{rc}, k_x\right) = \exp\left(-j\cdot\psi_{\text{res}}\left(k_{rc}, k_x\right)\right). \tag{19}$$

The echo signal is renovated as

$$\begin{aligned} &SS\left(k_r, k_x\right) \\ &= \exp\begin{pmatrix} -jR_0\cos\theta_e\sqrt{k_r^2\cos^2\theta_e - 2k_rk_x\sin\theta_e - k_x^2} \\ -j\left(R_0\sin\theta_e + x_n\right)\left(k_x + k_r\sin\theta_e\right)\end{pmatrix}. \end{aligned} \tag{20}$$

### C. Azimuth Resampling and 2-D Decoupling

After the spectrum rotation processing, the original range position $R_0$ will be renovated as $R_0' = R_0 + x_n\sin\theta_e$. Therefore, the signal is simultaneously updated to

$$\begin{aligned} &SS\left(k_r, k_x\right) = \exp \\ &\times\begin{pmatrix} -j\begin{pmatrix}\sin\theta_e\left(k_x + k_r\sin\theta_e\right) \\ +\cos\theta_e\sqrt{\begin{matrix}k_r^2\cos^2\theta_e \\ -2k_rk_x\sin\theta_e - k_x^2\end{matrix}}\end{pmatrix}R_0' \\ -j\begin{pmatrix}\cos\theta_e\left(k_x + k_r\sin\theta_e\right) \\ -\sin\theta_e\sqrt{\begin{matrix}k_r^2\cos^2\theta_e \\ -2k_rk_x\sin\theta_e - k_x^2\end{matrix}}\end{pmatrix}x_n\cos\theta_e\end{pmatrix}. \end{aligned} \tag{21}$$

From (21), there exists the azimuth dependence in the second exponential term due to the coupling between the quadratic term of azimuth wavenumber and azimuth position. In order to solve this issue, an azimuth wavenumber resampling method is performed, which yields

$$k_x' = \begin{pmatrix}\left(k_x + k_r\sin\theta_e\right) \\ -\sqrt{k_r^2\cos^2\theta_e - 2k_rk_x\sin\theta_e - k_x^2}\tan\theta_e\end{pmatrix}\cdot\cos\theta_e. \tag{22}$$

After azimuth resampling, the signal is rewritten as

$$SS(k_r, k_x') = \exp\left(-j\left(k_x'\cos\theta_e x_n + \sqrt{k_r^2 - {k_x'}^2}\cdot R_0'\right)\right). \tag{23}$$

Observing (23), it is evident that the azimuth dependence has been eliminated. Furthermore, only the first order of azimuth wavenumber $k_x'$ is related to the $x_n$.

In addition, the second exponential term contains range–azimuth coupling, which can be well decoupled through Stolt mapping. Hence, a reference function multiplication is introduced before employing Stolt mapping to accomplish bulk

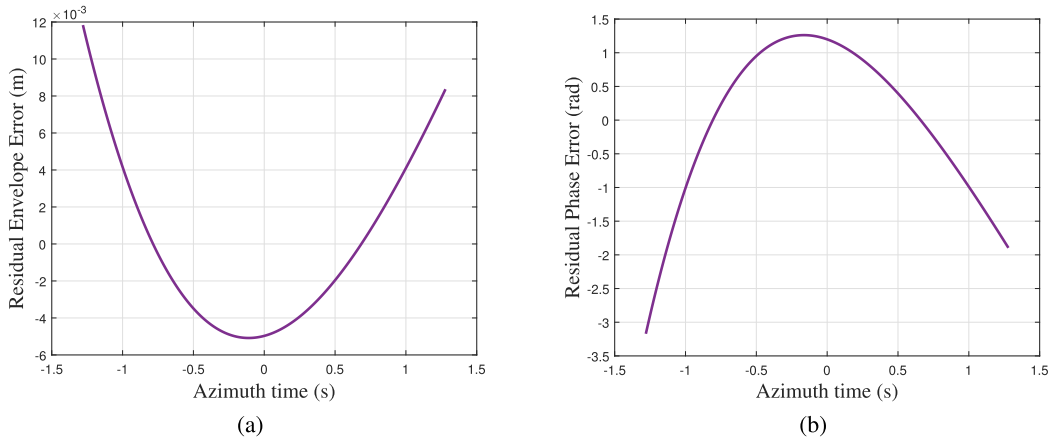


Fig. 5. Results of residual errors. (a) Result of residual envelope error. (b) Result of residual phase error.

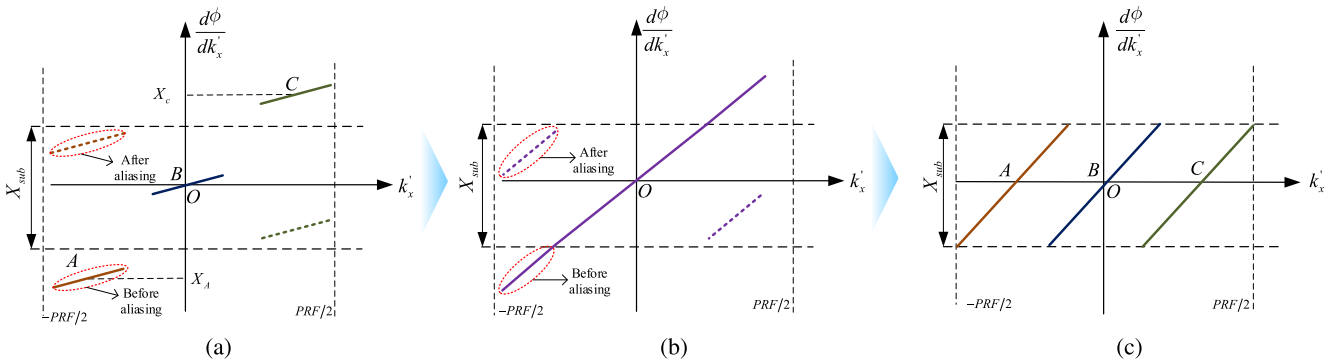


Fig. 6. Schematic diagram of data dealiasing operation. (a) Before dealiasing. (b) Data aligning. (c) After dealigning.

azimuth compression, which yields

$$H_{rcmc}\left(k_r, k_x'\right) = \exp\left(j\sqrt{k_r^2 - {k_x'}^2}\cdot R_s\right) \tag{24}$$

where $Rs$ is the reference range corresponding to the scene center. Then, the signal is expressed as

$$SS(k_r, k_x') = \exp\left(-j\left(k_x'\cos\theta_e x_n + \sqrt{k_r^2 - {k_x'}^2}\cdot\Delta R\right)\right) \tag{25}$$

where $\Delta R = R_0' - R_s$, and the modified Stolt mapping is designed as

$$k_y = \sqrt{k_r^2 - {k_x'}^2} - \sqrt{k_{rc}^2 - {k_x'}^2}. \tag{26}$$

After the modified Stolt interpolation, the signal is written as

$$SS(k_y, k_x') = \exp\left(-j\left[\begin{matrix}k_x'\cos\theta_e x_n \\ +\left(\sqrt{k_{rc}^2 - {k_x'}^2} + k_y\right)\cdot\Delta R\end{matrix}\right]\right). \tag{27}$$

Obviously, the 2-D coupling is eliminated, and only the linear term of range wavenumber $k_y$ exists in the range phase term.

### D. Data Aligning and Focusing Processing

In the condition of subaperture data processing, the interval of azimuth distance corresponds to short in highly squinted FMCW-SAR. Once the final image is focused on the 2-D time domain, the targets will be located at the wrong position, which will lead to the image aliasing. As shown in Fig. 6(a), the horizontal dimension represents the azimuth wavenumber axis. The vertical direction denotes the phase change rate axis corresponding to the azimuth wavenumber. Assuming that there exist three targets A, B, and C at one range unit. The time–frequency distribution lines (TFDLs) are presented, where the dashed TFDLs denote the real curves after aliasing, and the solid TFDLs represent the ideal curves before aliasing.

One method to eliminate image aliasing is to pad zeros in the azimuth time domain. However, it will extremely increase the computational burden in the high-squint SAR mode. Consequently, a more efficient method is needed. Therefore, (29) is multiplied by a uniform data aligning function, which yields

$$H_{\text{align}}\left(k_{rc}, k_x'\right) = \exp\left(-j\sqrt{k_{rc}^2 - {k_x'}^2}\cdot R_s\right). \tag{28}$$

The TFDLs are shown in Fig. 6(b). The dashed lines will be reflected in the opposite direction. Fig. 6(c) shows the final result of data aligning processing; it is evident that the azimuth aliasing

has been removed, which yields

$$SS(k_y, k_x') = \exp\left(-j\left(k_x' \cos\theta_e x_n + k_y \Delta R\right)\right) \cdot \exp\left(-j\sqrt{k_{rc}^2 - {k_x'}^2} \cdot R_0'\right). \quad (29)$$

At this moment, applying the range IFFT and the azimuth IFFT, the signal is renovated as

$$ss(R, X_a) = \mathrm{Sinc}\left(A_r\left(R - (R_0' - R_{\mathrm{ref}})\right)\right) \cdot \exp\left(-j\gamma_a (X_a - x_n \cos\theta_e)^2\right) \quad (30)$$

where $A_r$ is a constant value. $\gamma_a = 2\pi/(\lambda R_0')$ is the slope rate of the azimuth phase. It should be mentioned that the parabolic approximation principle is used in the above processing, namely, $4\pi/\lambda(\sqrt{{R_0'}^2 + (X_a - x_n\cos\theta_e)^2} - R_0') \approx 2\pi/\lambda R_0'(X_a - x_n\cos\theta_e)^2$. In order to select the azimuth wavenumber domain as the final focusing domain, the second-order-deramp function is given by

$$H_{\mathrm{deramp}}(X_a) = \exp\left(j\gamma_a X_a^2\right). \quad (31)$$

After azimuth deramp processing, the signal is expressed as

$$ss(R, X_a) = \mathrm{Sinc}\left(A_r\left(R - (R_0' - R_{\mathrm{ref}})\right)\right) \cdot \exp\left(j\gamma_a x_n \cos\theta_e X_a\right) \cdot \exp\left(-j\gamma_a \cos^2\theta_e x_n^2\right) \quad (32)$$

where the first exponential is only related to the linear term of the azimuth position, and the second exponential denotes the geometric deformation. Then, performing azimuth FFT, the signal becomes

$$sS(R, k_x') = \mathrm{Sinc}\left(A_r\left(R - (R_0' - R_{\mathrm{ref}})\right)\right) \cdot \mathrm{Sinc}\left(A_a\left(k_x' - \gamma_a x_n \cos\theta_e\right)\right) \cdot \exp\left(-j\gamma_a \cos^2\theta_e x_n^2\right) \quad (33)$$

where $A_a$ is a constant related to small-aperture length. Fig. 7 shows the flowchart of the proposed algorithm.

## IV. Computational Cost Analysis

As mentioned above, the proposed algorithm mainly includes four procedures.

1) SC and rotation;
2) residual phase components compensation;
3) the azimuth resampling and 2-D decoupling;
4) the data aligning and focusing processing.

Hence, in order to further analyze the computational complexity of the proposed algorithm, the computation cost is discussed here in detail.

Assuming that the processed echo data are a matrix of $N_r \times N_a$ size, where $N_r$ and $N_a$ denote the sample points in the range and azimuth direction, respectively. As shown in Fig. 7, the whole imaging algorithm includes one interpolation, seven complex multiplications, and five FFTs. According to the authors in [38] and [39], one interpolation needs $2(2M_{\mathrm{ker}} - 1)N_r N_a$ operations, for each complex multiplication needs $6N_r N_a$ operations, and the floating-point process of each FFT can be derived as $5N_r N_a \log_2[N_{r/a}]$. Consequently, the computation load of the whole procedure can be calculated as

$$S = 42N_r N_a + 4\left(2M_{\mathrm{ker}} - 1\right)N_r N_a + 10N_r N_a \log_2\left(N_r\right) + 15N_r N_a \log_2\left(N_a\right) \quad (34)$$

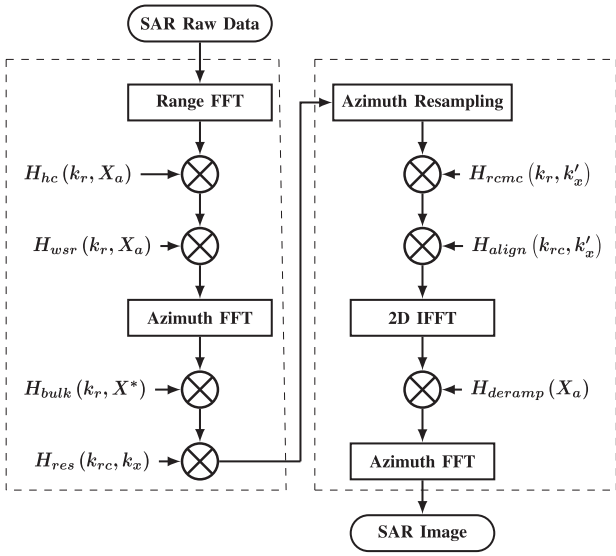


Fig. 7. Flowchart of the proposed algorithm.

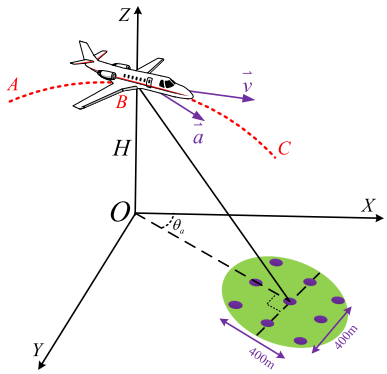


Fig. 8. Highly squinted FMCW-SAR geometry and target distribution.

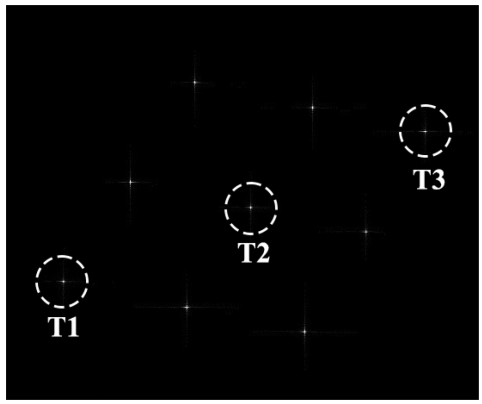


Fig. 9. Imaging results of point targets by the proposed method.

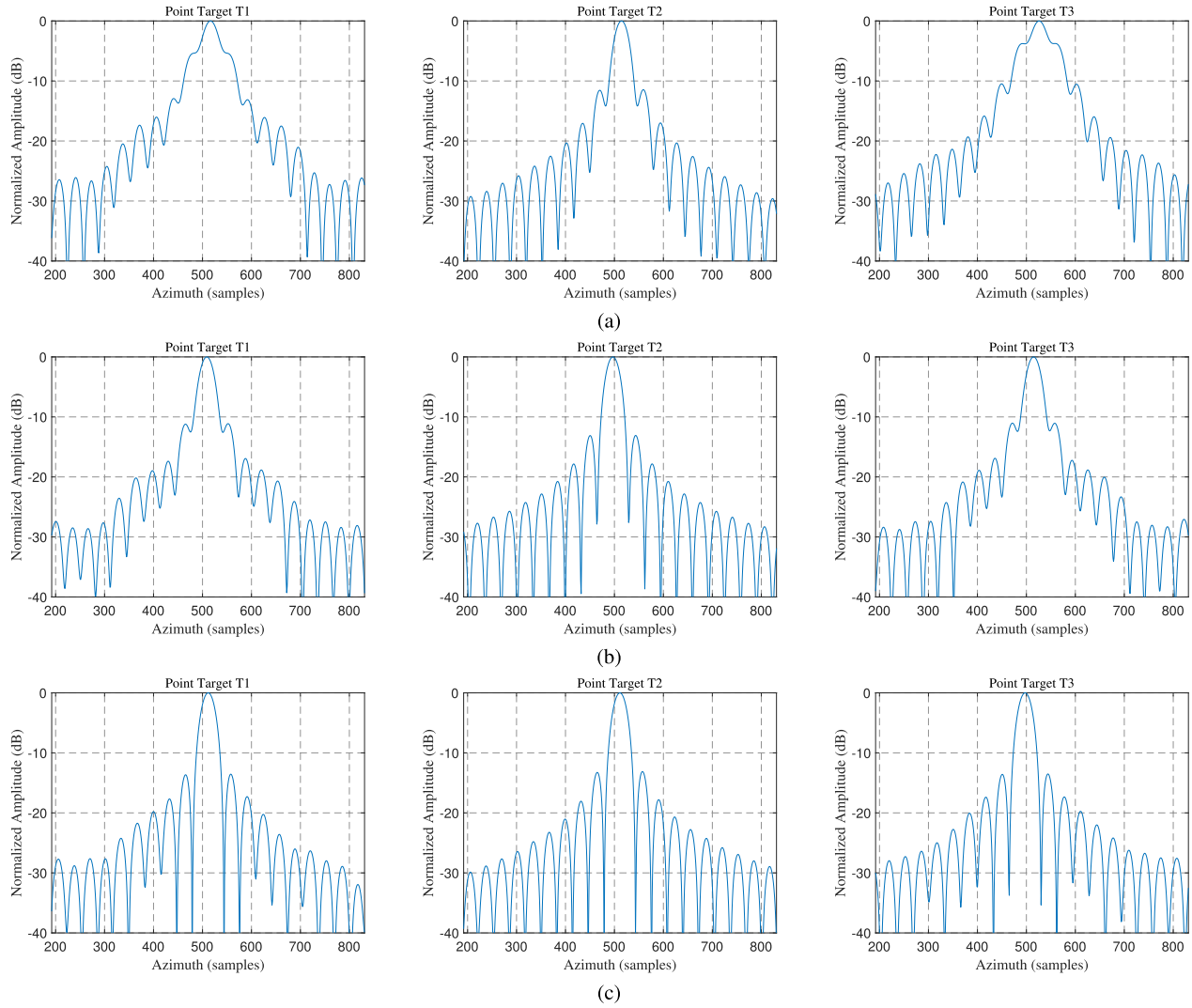


Fig. 10. Azimuth profiles of targets T1–T3 processed by different methods. (a) Modified RD method. (b) Wavenumber-domain method. (c) Proposed method.

which is of order $O(N^2 \log_2 N)$, where $N$ is the 1-D size of the echo data. $M_{\text{ker}}$ denotes the interpolation kernel.

## V. Simulation and Raw Data Processing

### A. Numerical Simulation

In this section, the numerical simulations are performed to further demonstrate the effectiveness of the proposed algorithm. The numerical simulations use a highly squinted FMCW-SAR with a curved configuration, as shown in Fig. 8. The simulation parameters are listed in Table I. The uniform scattering of point targets on the ground is a $3 \times 3$ matrix. The whole scene is about 400 m in the range and azimuth direction. Fig. 9 shows the numerical simulation result achieved by the proposed algorithm. The range resolution and the azimuth resolution are both about 0.15 m.

In order to better evaluate the superiority of the proposed algorithm, a comparison of the proposed algorithm with the modified RD method [15] and the wavenumber method [27] by the numerical simulation is implemented, as shown in Fig. 10. The azimuth profiles of points T1–T3 achieved by the modified RD method are shown in Fig. 10(a); although the continuous motion has been removed, the high-order 2-D coupling phase terms introduced by high-squint angle are not considered. Hence, targets T1 and T3 are seriously defocused. Fig. 10(b) displays the azimuth profiles of targets T1–T3 achieved by the wavenumber-domain method. The range-dependent second- and higher order range–azimuth coupling components in the high-squint case have been well analyzed and considered. However, the variation of velocity is ignored in its range model. Therefore, targets T1 and T3 are defocused. The azimuth profiles of targets T1–T3 achieved by the proposed algorithm are given in Fig. 10(c). Because the 3-D acceleration is considered in the range model, the azimuth dependence is removed by the azimuth resampling approach, and the modified Stolt interpolation removes the range–azimuth coupling term. Consequently, targets T1–T3 are well focused.

Furthermore, for further quantitative analysis, the performance parameters of peak sidelobe ratio (PSLR) and integrated sidelobe (ISLR) of the three methods are given in Table II. The proposed method's performance parameters are close to the

TABLE II
AZIMUTH PERFORMANCE ANALYSIS OF SELECTED TARGETS

| Target | Method | Azimuth | |
|---|---|---|---|
| | | PSLR/dB | ISLR/dB |
| T1 | The first reference method | -5.36 | -3.45 |
| | The second reference method | -8.12 | -7.91 |
| | The proposed method | -13.34 | -9.85 |
| T2 | The first reference method | -11.45 | -8.42 |
| | The second reference method | -12.46 | -9.35 |
| | The proposed method | -13.12 | -9.79 |
| T3 | The first reference method | -3.76 | -5.27 |
| | The second reference method | -7.13 | -6.96 |
| | The proposed method | -13.35 | -9.86 |

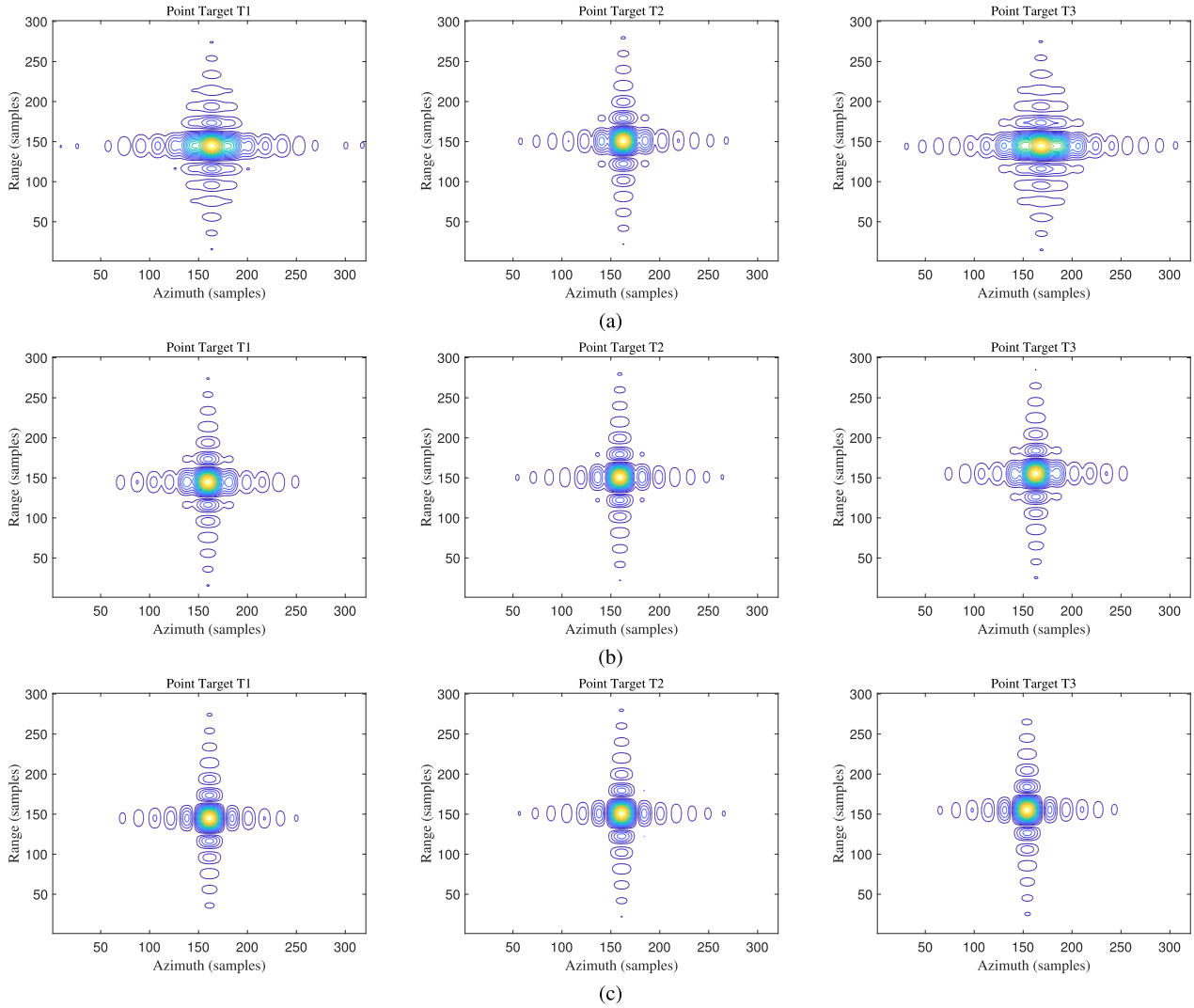


Fig. 11. Contour plots of targets T1–T3 processed by different methods. (a) Modified RD method. (b) Wavenumber-domain method. (c) Proposed method.

TABLE III
AZIMUTH PERFORMANCE ANALYSIS OF ISOLATED TARGETS

| Method | Azimuth | | Image sharpness |
|---|---|---|---|
| | PSLR/dB | ISLR/dB | |
| The modified RD method | -6.23 | -1.96 | 3.72e25 |
| The wavenumber-domain method | -10.37 | -6.74 | 6.39e25 |
| The proposed method | -12.82 | -9.13 | 3.65e26 |

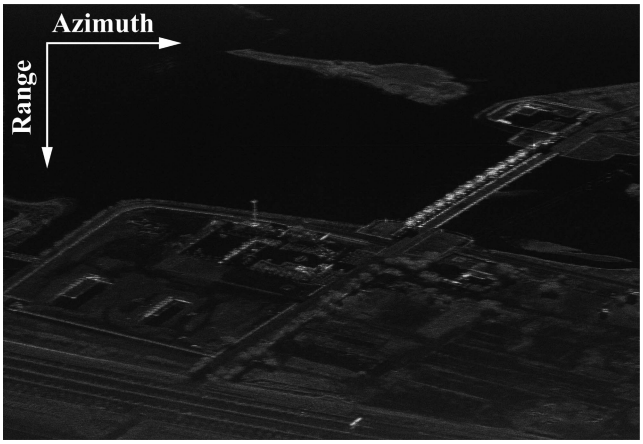


Fig. 12. Result of raw data processed by the modified RD method.

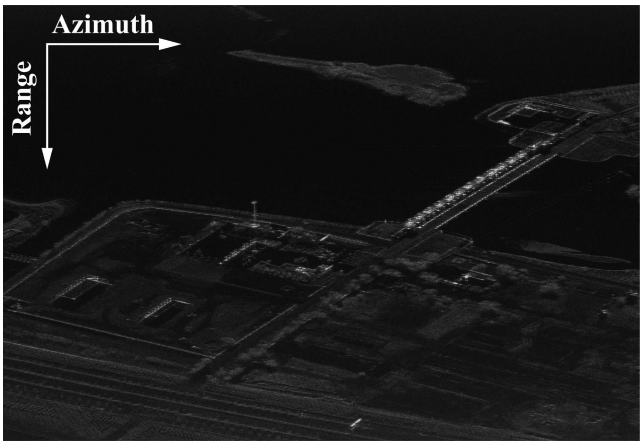


Fig. 13. Result of raw data processed by the wavenumber-domain method.

theoretical values of PSLR ($-13.2$ dB) and ISLR ($-9.8$ dB). In addition, to fully demonstrate the performance of the proposed method, the contour plots of targets T1–T3 achieved by three methods are compared in Fig. 11. It can be easily found that the results of the modified RD method [17] are worst. The targets T1 and T3 are completely defocused, as shown in Fig. 11(a). The wavenumber-domain method [30] results are given in Fig. 11(b). It is obvious that the main lobes and sidelobes of the targets T1 and T3 are coupled with each other. Fig. 11(c) shows the contour plots of the proposed algorithm. The main lobe and sidelobes of three targets, T1–T3, are well separated from each other and

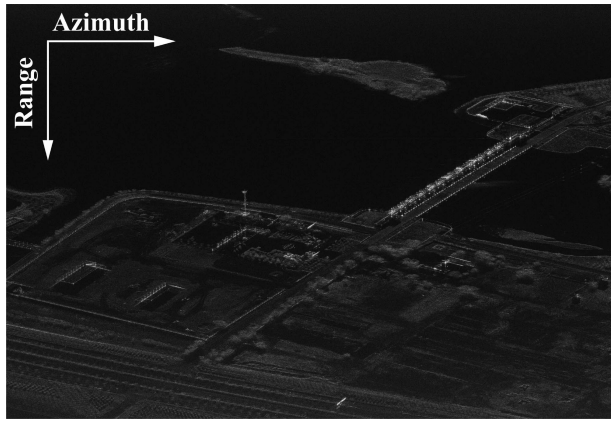


Fig. 14. Results of real data processed by the proposed method.

present an ideal "cross," which validates the excellent focusing performance.

### B. Raw Data Processing

In the following, the raw-measured data processing is implemented on the highly squinted FMCW-SAR with a curved trajectory. The FMCW-SAR system works at strip-map mode with ka-band.

The system has a range bandwidth of 1.2 GHz. The squint angle is about $40^\circ$. The center slant range is about 1.6 km. The velocity and acceleration vectors of transmitter are about $(82.26, 0.36, -4.21)$ m/s and $(0.61, 0.23, -1.82)$ m/s$^2$, respectively. The image scene is about 600 m in the range direction and 420 m in the cross-range direction. The range resolution and cross-range resolution are both about 0.15 m. Then, a comparison of the modified RD method [18], the wavenumber-domain method [32], and the proposed method is made.

The result of real data achieved by the RD method is given in Fig. 12. Because the high-order 2-D coupling phase terms are neglected; thus, it cannot deal with highly squinted FMCW SAR data. Fig. 13 gives the result of real data processed by the wavenumber-domain method. Although the high-order range–azimuth coupling components have been removed, its range model does not consider the velocity variation. Consequently, some residual phase errors introduced by the acceleration exist, which make the final image defocused, as shown in Fig. 15(b). Fig. 14 displays the results of real data processed by the proposed method. Because the velocity variation is considered in the range

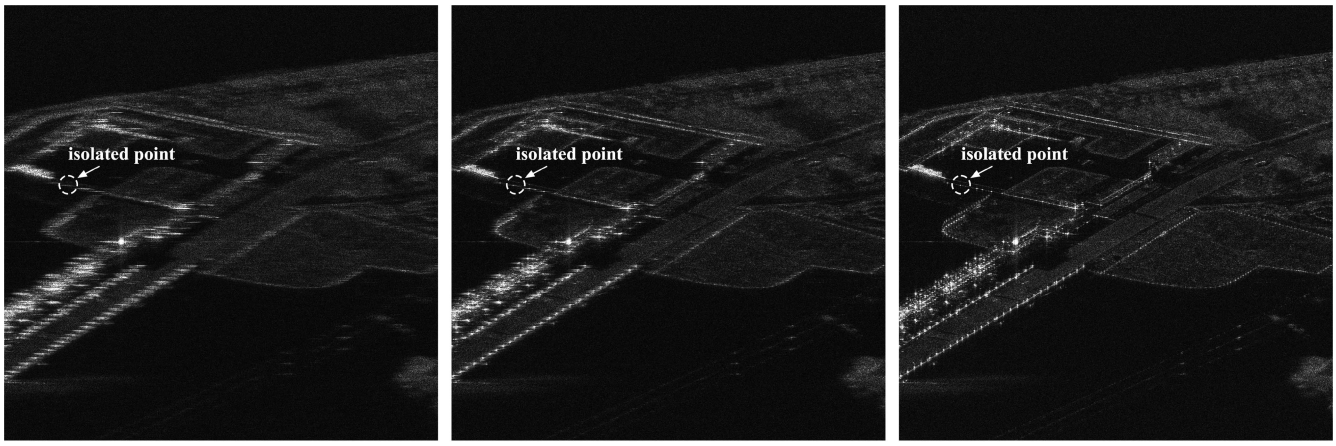


Fig. 15. Comparison of the selected subdomain. (a) Result processed by the modified RD method. (b) Result processed by the wavenumber-domain method. (c) Result processed by the proposed method.

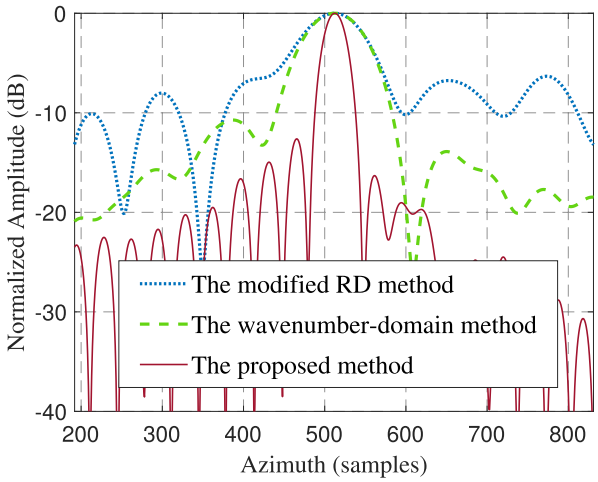


Fig. 16. Image contrast of isolated point.

model, the issue of azimuth dependence is solved by azimuth resampling, and the modified Stolt interpolation removes the range–azimuth coupling term. Consequently, the final image is well focused, and the image details have been well preserved, as shown in Fig. 15(c).

In addition, to further demonstrate the effectiveness of the proposed method, the comparison of the selected subdomain is shown in Fig. 15(c). The white dashed circle chooses an isolated point, and its azimuth impulse response via the three methods mentioned above is shown in Fig. 16. Furthermore, the performance parameters' of PSLR and ISLR of the three methods are given in Table III. It is obvious that the proposed method achieves the best image performance.

## VI. Conclusion

This article develops a modified wavenumber-domain algorithm for highly squinted FMCW-SAR with a curved trajectory. First, the 3-D acceleration is considered in the modified range model. Then, the SC and rotation operations are performed to guarantee the 2-D WS. Afterward, the residual phase terms introduced by acceleration are bulk compensated for. Subsequently, the azimuth resampling and the modified Stolt interpolation methods are adopted to eliminate the azimuth dependence and the 2-D coupling, respectively. Moreover, to avoid padding zeros, the azimuth wavenumber domain is selected to focus the final image through data aligning processing. Finally, the numerical simulation and raw-measured FMCW-SAR data processing are performed to demonstrate the superiority of the proposed algorithm.

## References

[1] Z. Bao, M. Xing, and T. Wang, *Radar Imaging Techniques*. Beijing, China: Publishing House Electron. Ind., 2006.
[2] I. G. Cumming and F. H. Wong, *Digital Processing of Synthetic Aperture Radar Data: Algorithms and Implementation*. Boston, MA, USA: Artech House, 2005.
[3] Y. Liu et al., "Echo model analyses and imaging algorithm for high resolution SAR on high-speed platform," *IEEE Trans. Geosci. Remote Sens.*, vol. 50, no. 3, pp. 933–950, Mar. 2012.
[4] S. Chen, H. Zhao, S. Zhang, and Y. Chen, "An extended non-linear chirp scaling algorithm for missile borne SAR imaging," *Signal Process.*, vol. 99, pp. 58–68, Jun. 2014.
[5] S. Tang et al., "Processing of monostatic SAR data with general configurations," *IEEE Trans. Geosci. Remote Sens.*, vol. 53, no. 12, pp. 6529–6546, Dec. 2015.
[6] Y. Wu, G.-C. Sun, C. Yang, J. Yang, M. Xing, and Z. Bao, "Processing of very high resolution spaceborne sliding spotlight SAR data using velocity scaling," *IEEE Trans. Geosci. Remote Sens.*, vol. 54, no. 3, pp. 1505–1518, Mar. 2016.
[7] B. Deng, X. Li, H. Wang, Y. Qin, and J. Wang, "Fast raw-signal simulation of extended scenes for missile-borne SAR with constant acceleration," *IEEE Geosci. Remote Sens. Lett.*, vol. 8, no. 1, pp. 44–49, Jan. 2011.
[8] T. Zeng, Y. Li, Z. Ding, T. Long, D. Yao, and Y. Sun, "Subaperture approach based on azimuth-dependent range cell migration correction and azimuth focusing parameter equalization for maneuvering high-squint-mode SAR," *IEEE Trans. Geosci. Remote Sens.*, vol. 52, no. 12, pp. 6718–6734, Dec. 2015.
[9] S.-X. Zhang, M.-D. Xing, and K. Zhang, "Characteristics analysis and image processing for full-polarization synthetic aperture radar based on electromagnetic scattering from flat horizontal perfect electric conducting reflector," *IEEE Trans. Geosci. Remote Sens.*, vol. 56, no. 1, pp. 313–327, Jan. 2018.

[10] J. Chen, J. Zhang, Y. Jin, H. Yu, B. Liang, and D.-G. Yang, "Real-time processing of spaceborne SAR data with nonlinear trajectory based on variable PRF," *IEEE Trans. Geosci. Remote Sens.*, vol. 60, 2022, Art. no. 5205212.
[11] J. Chen, M. Xing, H. Yu, B. Liang, J. Peng, and G.-C. Sun, "Motion compensation/autofocus in airborne synthetic aperture radar: A review," *IEEE Geosci. Remote Sens. Mag.*, vol. 10, no. 1, pp. 185–206, Mar. 2022.
[12] C. Jianlai and Y. U. Hanwen, "Wide-beam SAR autofocus based on blind resampling," *Sci. China Inf. Sci.*, vol. 66, 2023, Art. no. 140304.
[13] G. L. Charvat and L. C. Kempel, "Synthetic aperture radar imaging using a unique approach to frequency-modulated continuous-wave radar design," *IEEE Antennas Propag. Mag.*, vol. 48, no. 1, pp. 171–177, Feb. 2006.
[14] T. Zhang, Y. Li, J. Wang, M. Xing, L. Guo, and P. Zhang, "A modified range model and extended omega-K algorithm for high-speed-high-squint SAR with curved trajectory," *IEEE Trans. Geosci. Remote Sens.*, vol. 61, Mar. 2023, Art. no. 5204515, doi: 10.1109/TGRS.2023.3255518.
[15] H. Lin et al., "Time-domain autofocus for ultrahigh resolution SAR based on azimuth scaling transformation," *IEEE Trans. Geosci. Remote Sens.*, vol. 60, May 2022, Art. no. 5227812.
[16] J. J. M. De Wit, A. Meta, and P. Hoogeboom, "Modified range-Doppler processing for FM-CW synthetic aperture radar," *IEEE Geosci. Remote Sens. Lett.*, vol. 3, no. 1, pp. 83–87, Jan. 2006.
[17] A. Meta, P. Hoogeboom, and L. P. Ligthart, "Signal processing for FMCW SAR," *IEEE Trans. Geosci. Remote Sens.*, vol. 45, no. 11, pp. 3519–3532, Nov. 2007.
[18] A. Meta, P. Hoogeboom, and L. P. Ligthart, "Non-linear frequency scaling algorithm for FMCW SAR data," in *Proc. Eur. Radar Conf.*, Manchester, U.K., 2006, pp. 9–12.
[19] Y. Xiong, B. Liang, H. Yu, J. Chen, Y. Jin, and M. Xing, "Processing of bistatic SAR data with nonlinear trajectory using a controlled-SVD algorithm," *IEEE J. Sel. Topics Appl. Earth Observ. Remote Sens.*, vol. 14, pp. 5750–5759, May 2021.
[20] G. Sun, M. Xing, Y. Liu, L. Sun, Z. Bao, and Y. Wu, "Extended NCS based on method of series reversion for imaging of highly squinted SAR," *IEEE Geosci. Remote Sens. Lett.*, vol. 8, no. 3, pp. 446–450, May 2011.
[21] G.-C. Sun, X. Jiang, M. Xing, Z.-J. Qiao, Y. Wu, and Z. Bao, "Focus improvement of highly squinted data based on azimuth nonlinear scaling," *IEEE Trans. Geosci. Remote Sens.*, vol. 49, no. 6, pp. 2308–2322, Jun. 2011.
[22] S.-X. Zhang, M.-D. Xing, X.-G. Xia, L. Zhang, R. Guo, and Z. Bao, "Focus improvement of high-squint SAR based on azimuth dependence of quadratic range cell migration correction," *IEEE Geosci. Remote Sens. Lett.*, vol. 10, no. 1, pp. 150–154, Jan. 2013.
[23] D. An, X. Huang, T. Jin, and Z. Zhou, "Extended non-linear chirp scaling algorithm for high-resolution highly squint SAR data focusing," *IEEE Trans. Geosci. Remote Sens.*, vol. 50, no. 9, pp. 3595–3609, Sep. 2012.
[24] Y. Liang, Z. Y. Li, L. Zeng, M. D. Xing, and Z. Bao, "A high-order phase correction approach for focusing HS-SAR small-aperture data of high-speed moving platforms," *IEEE J. Sel. Topics Appl. Earth Observ. Remote Sens.*, vol. 8, no. 9, pp. 4551–4561, Sep. 2015.
[25] C. Cafforio, C. Prati, and F. Rocca, "SAR data focusing using seismic migration techniques," *IEEE Trans. Aerosp. Electron. Syst.*, vol. 27, no. 2, pp. 194–207, Mar. 1991.
[26] R. Wang, O. Loffeld, H. Nies, and J. Ender, "Focusing spaceborne/airborne hybrid bistatic SAR data using wavenumber-domain algorithm," *IEEE Trans. Geosci. Remote Sens.*, vol. 47, no. 7, pp. 2275–2283, Jul. 2009.
[27] L. Zhang, J. Sheng, M. Xing, Z. Qiao, T. Xiong, and Z. Bao, "Wavenumber-domain autofocusing for highly squinted UAV SAR imagery," *IEEE Sensors J.*, vol. 12, no. 5, pp. 1574–1588, May 2012.
[28] T. Xiong, M. Xing, X. Xia, and Z. Bao, "New applications of Omega-K algorithm for SAR data processing using effective wavelength at high squint," *IEEE Trans. Geosci. Remote Sens.*, vol. 51, no. 5, pp. 3156–3169, May 2013.
[29] Y. Li, T. Zhang, H. Mei, Y. Quan, and M. Xing, "Focusing translational-variant bistatic forward-looking SAR data using the modified omega-K algorithm," *IEEE Trans. Geosci. Remote Sens.*, vol. 60, 2022, Art. no. 5203916, doi: 10.1109/TGRS.2021.3063780.
[30] R. Wang, O. Loffeld, H. Nies, S. Knedlik, M. Hagelen, and H. Essen, "Focus FMCW SAR data using the wavenumber domain algorithm," *IEEE Trans. Geosci. Remote Sens.*, vol. 48, no. 4, pp. 2109–2118, Apr. 2010, doi: 10.1109/TGRS.2009.2034368.
[31] L. Huang, X. Qiu, D. Hu, and C. Ding, "Focusing of medium-Earth-orbit SAR with advanced non-linear chirp scaling algorithm," *IEEE Trans. Geosci. Remote Sens.*, vol. 49, no. 1, pp. 500–508, Jan. 2011.
[32] Z. Li et al., "An improved range model and omega-K-based imaging algorithm for high-squint SAR with curved trajectory and constant acceleration," *IEEE Geosci. Remote Sens. Lett.*, vol. 13, no. 5, pp. 656–660, May 2016.
[33] M. Bao, M. D. Xing, Y. Wang, and Y. C. Li, "Two-dimensional spectrum for MEO SAR processing using a modified advanced hyperbolic range equation," *Electron. Lett.*, vol. 47, no. 18, pp. 1043–1045, Sep. 2011.
[34] P. Wang, W. Liu, J. Chen, M. Niu, and W. Yang, "A high-order imaging algorithm for high-resolution spaceborne SAR based on a modified equivalent squint range model," *IEEE Trans. Geosci. Remote Sens.*, vol. 53, no. 3, pp. 1225–1235, Mar. 2015.
[35] A. F. Yegulalp, "Fast backprojection algorithm for synthetic aperture radar," in *Proc. IEEE Radar Conf.*, Waltham, MA, USA, 1999, pp. 60–64.
[36] L. M. H. Ulander, H. Hellsten, and G. Stenstrom, "Synthetic-aperture radar processing using fast factorized back-projection," *IEEE Trans. Aerosp. Electron. Syst.*, vol. 39, no. 3, pp. 760–776, Jul. 2003.
[37] L. Zhang, H. L. Li, Z. J. Qiao, and Z. W. Xu, "A fast BP algorithm with WS fusion for high-resolution spotlight SAR imaging," *IEEE Geosci. Remote Sens. Lett.*, vol. 11, no. 9, pp. 1460–1464, Sep. 2014.
[38] Y. Li, G. Xu, S. Zhou, M. Xing, and X. Song, "A novel CFFBP algorithm with noninterpolation image merging for bistatic forward-looking SAR focusing," *IEEE Trans. Geosci. Remote Sens.*, vol. 60, Mar. 2022, Art. no. 5225916, doi: 10.1109/TGRS.2022.3162230.
[39] G. Xu, S. Zhou, L. Yang, S. Deng, Y. Wang, and M. Xing, "Efficient fast time-domain processing framework for airborne bistatic SAR continuous imaging integrated with data-driven motion compensation," *IEEE Trans. Geosci. Remote Sens.*, vol. 60, 2022, Art. no. 5208915, doi: 10.1109/TGRS.2021.3099204.
[40] H. W. Mei, Z. Q. Meng, M. Q. Liu, Y. C. Li, and Y. H. Quan, "Thorough understanding property of bistatic forward-looking high-speed maneuvering-platform SAR," *IEEE Trans. Aerosp. Electron. Syst.*, vol. 53, no. 4, pp. 1826–1845, Aug. 2017.
[41] H. Mei, Y. Li, M. Xing, Y. Quan, and C. Wu, "A frequency-domain imaging algorithm for translational variant bistatic forward-looking SAR," *IEEE Trans. Geosci. Remote Sens.*, vol. 58, no. 3, pp. 1502–1515, Mar. 2020, doi: 10.1109/TGRS.2019.2943743.

**Tinghao Zhang** (Graduate Student Member, IEEE) was born in Xianyang, China, in 1996. He received the B.S. degree in electronic and information engineering in 2018 from Xi'an University of Technology, Xi'an, China, where he is currently working toward the Ph.D. degree in signal processing with the National Laboratory of Radar Signal Processing.

He is currently the Vice Chair of the IEEE GRSS Xidian University student branch chapter. His research interests include monostatic/bistatic SAR imaging and motion compensation.

**Yachao Li** (Member, IEEE) was born in Jiangxi Province, China, in 1981. He received the M.S. and Ph.D. degrees in electrical engineering from Xidian University, Xi'an, China, in 2005 and 2008, respectively.

He is currently a Professor with Xidian University. His current research interests include SAR/ISAR imaging, missileborne SAR imaging, ground-moving target indication, matching and orientation of SAR image, real-time signal processing based on FPGA and DSP technology, and distributed radar.

**Mingze Yuan** was born in Shaanxi, China, in 1997. He received the B.S. degree in remote sensing science and technology in 2020 from Xidian University, Xi'an, China, where he is currently working toward the M.S. degree with the National Laboratory of Radar Signal Processing.

His research interests include radar signal processing and SAR imaging.

**Liang Guo** (Member, IEEE) was born in Henan, China, in 1983. He received the B.S. degree and the Ph.D. degree in signal and information processing from Xidian University, Xi'an, China, in 2005 and 2009, respectively.

He is currently a Full Professor with the School of Optoelectronic Engineering, Xidian University. His research interests include imaging of several synthetic aperture radar modes, synthetic aperture radar, and real-time imaging.

**Jiao Guo** received the B.S. degree in electronic information engineering and the Ph.D. degree in information and communication engineering from Xidian University, Xi'an, China, in 2006 and 2011, respectively.

From 2015 to 2016, he was a Visiting Scholar with CSIRO Data61, Floreat, WA, Australia. He is currently an Associate Professor with the College of Mechanical and Electronic Engineering, Northwest A&F University, Xianyang, China. His research interests include radar remote sensing, polarimetric synthetic aperture radar (PolSAR), SAR interferometry, and PoISAR interferometry.

**Hao Lin** (Student Member, IEEE) was born in Zhejiang, China, in 1996. He received the B.S. degree in intelligent science and technology in 2018 from Xidian University, Xi'an, China, where he is currently working toward the Ph.D. degree in signal processing with the National Laboratory of Radar Signal Processing.

His research interests include synthetic aperture radar (SAR) imaging, SAR motion compensation, and SAR interference suppression.

**Mengdao Xing** (Fellow, IEEE) was born in Zhejiang, China, in 1975. He received the B.S. and Ph.D. degrees in electrical engineering from Xidian University, Xi'an, China, in 1997 and 2002, respectively.

He is currently a Full Professor with the National Laboratory of Radar Signal Processing, Xidian University. He is also with the National Key Laboratory of Microwave Imaging Technology, Institute of Electronics, Chinese Academy of Sciences, Beijing, China. He is the author or coauthor of two books and has authored or coauthored more than 200 papers. His research interests include synthetic aperture radar (SAR), inverse SAR, and sparse signal processing.